JACS
JOURNAL OF THE AMERICAN CHEMICAL SOCIETY

Article

pubs.acs.org/JACS

Direct Access to Hierarchically Porous Inorganic Oxide Materials with Three-Dimensionally Interconnected Networks

Jongkook Hwang,[†] Changshin Jo,[†] Kahyun Hur,[‡] Jun Lim,[§] Seongseop Kim,[†] and Jinwoo Lee*[,†]

[†]Department of Chemical Engineering, Pohang University of Science and Technology (POSTECH), Pohang 790-784, Republic of Korea

[‡]Center for Computational Science, Korea Institute of Science and Technology (KIST), Seoul 136-791, Republic of Korea

[§]Beamline Division, Pohang Light Source, Pohang 790-784, Republic of Korea

Supporting Information

ABSTRACT: Hierarchically porous oxide materials have immense potential for applications in catalysis, separation, and energy devices, but the synthesis of these materials is hampered by the need to use multiple templates and the associated complicated steps and uncontrollable mixing behavior. Here we report a simple one-pot strategy for the synthesis of inorganic oxide materials with multiscale porosity. The inorganic precursor and block copolymer are coassembled into an ordered mesostructure (microphase separation), while the in situ-polymerized organic precursor forms organic-rich macrodomains (macrophase separation) around which the mesostructure grows. Calcination generates hierarchical meso/macroporous SiO_2 and TiO_2 with three-dimensionally interconnected pore networks. The continuous 3D macrostructures were clearly visualized by nanoscale X-ray computed tomography. The resulting TiO_2 was used as the anode in a lithium ion battery and showed excellent rate capability compared with mesoporous TiO_2. This work is of particular importance because it (i) expands the base of BCP self-assembly from mesostructures to complex porous structures, (ii) shows that the interplay of micro- and macrophase separation can be fully exploited for the design of hierarchically porous inorganic materials, and therefore (iii) provides strategies for researchers in materials science and polymer science.

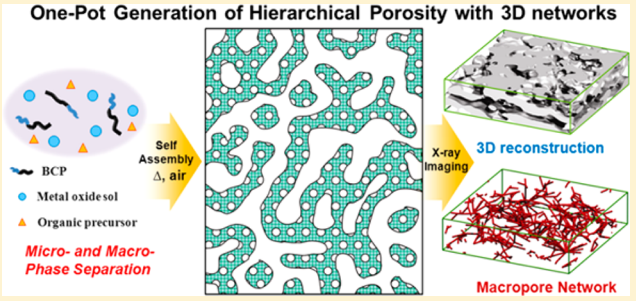

INTRODUCTION

The structural hierarchies found in nature have a remarkable variety of unique properties, inspiring the development of new materials with multiscale structures and multiple functions.[1] Materials with hierarchical porosity simultaneously combine the benefits of the different pore size regimes, providing highly improved mass transport through macropores coupled with high specific surface area due to the presence of micropores and mesopores.[2] In particular, inorganic oxide materials with well-defined pore networks on multiple length scales have immense potential for applications in separation,[3] catalysis,[4] and energy conversion and storage.[5]

A wide variety of mesoporous materials with different compositions and morphologies have been synthesized by direct precipitation,[6] true liquid-crystal templating,[7] exotemplating,[8] and evaporation-induced self-assembly (EISA).[9] Combinations of these conventional routes for fabrication of mesostructures with macroscale templates such as biological species,[10] foams,[11] and colloidal crystals[12] have been adopted to create materials with hierarchical porosity. In particular, the block copolymer (BCP)-based EISA pathway has been demonstrated to be an efficient strategy to produce hierarchically porous oxides in the form of film, fiber, powder, and monolith.[13] For example, a sequential approach using post-infiltration of the BCP and precursor into preformed colloidal crystals (e.g., polystyrene or silica beads) enables the construction of various kinds of ordered meso/macroporous materials.[13b−e] However, this approach requires laborious and complicated steps, including large-scale preparation of colloidal crystals, packing of synthesized colloids, and infiltration of the BCP and precursor into the voids of packed colloids; furthermore, the precursor cannot be easily prevented from precipitating or from aggregating away from the colloidal templates. As an alternative approach, multiple templates with different length scales have been used simultaneously.[13f−h] However, these templates mix uncontrollably and work competitively rather than cooperatively, thereby frequently resulting in single pore sizes or poorly defined disordered nanostructures.

When a homogeneous mixture crosses the phase boundary (spinodal line) into the unstable region of the phase diagram, phase separation by spinodal decomposition (SD) occurs.[14] SD can be induced by temperature changes, solvent removal/addition, pressure changes, and chemical reaction.[3,14,15] Because SD generates interspersed macrophases with distinct

Received: September 4, 2014
Published: October 22, 2014

   dx.doi.org/10.1021/ja5091172 | J. Am. Chem. Soc. 2014, 136, 16066−16072

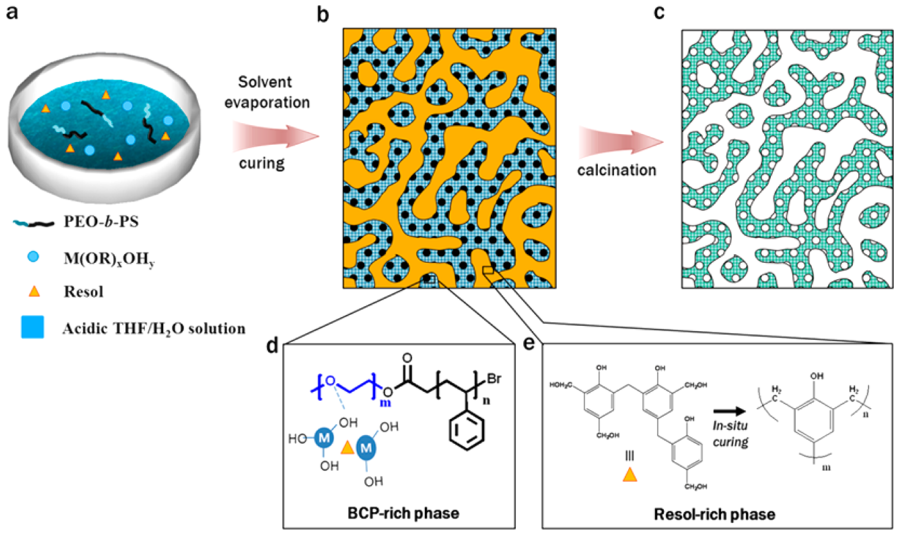

Figure 1. (a–c) Schematic representation of combined hierarchical assembly of micro- and macrophase separation (CHAMPS): (a) blend of metal alkoxide, resol, and PEO-*b*-PS dissolved in acidic THF/H_2O solution; (b) phase separation upon solvent evaporation and thermal annealing; (c) formation of hierarchical porosity after calcination. (d) Illustration of the structure of the M–OH/BCP-rich phase where the ordered mesostructure develops. Hydrolyzed M–OH species selectively interact with the PEO block through hydrogen bonding. It should be noted that some portions of the resol also coassembles with the BCP. (e) Formation of the resol-rich phase by in situ curing upon self-assembly.

chemical compositions, selective removal of one phase leaves continuous macropores in the other phase. Recently, hierarchically porous polymer scaffolds were fabricated using dual-phase separation based on SD.[16] This process exploits SD driven by rapid thermal quenching at temperatures above 100 °C. This temperature control could limit the potential applicability of this approach with inorganic precursors that are highly reactive, as it would result in the formation of large, highly aggregated particles as a result of uncontrollable inorganic condensation reactions. Therefore, the development of a simple yet controllable pathway for the fabrication of robust and functional inorganic materials with multiscale porosity is still highly desirable.

Blends of BCPs and multiple precursors have been extensively used to prepare inorganic mesoporous materials; those blends usually show complicated phase behavior that frequently induces macrophase separation of large domains (>50 nm).[17] During cooperative assembly of multicomponent mixtures, segregation at the macroscale tends to occur because of solubility limits, differences in growth kinetics, and interactions among precursors.[17,18] Mostly, macrophase separation has been regarded as an undesirable behavior that should be suppressed or eliminated because it usually causes deformation of the mesostructure, yielding poorly ordered frameworks.[17b,18c,19]

From a different viewpoint, tailoring the macrophase separation enables another regime of nanoengineering that has been neglected: the direct synthesis of hierarchical nanostructures. We expect that the interplay between micro- and macrophase separation can offer an opportunity to produce complex but interesting structures, presenting a new way of synthesizing hierarchically porous inorganic materials. We have designed a new system, combined hierarchical assembly of micro- and macrophase separation (CHAMPS), that is based on a blend of BCP–organic–inorganic precursor that undergoes macrophase separation into an organic-rich phase and a BCP–inorganic-rich phase in which ordered mesostructure develops by microphase separation. Continuous macropores are created by calcination to remove the organic macrodomains.

In this work, we demonstrated the straightforward synthesis of hierarchically porous SiO_2 and TiO_2 with 3D interconnected networks. We thoroughly investigated the unique structure formation process and mechanism associated with in situ polymerization of organic additives. The complex, disordered 3D macrostructures were reconstructed and quantitatively assessed using nanoscale X-ray computed tomography. As a proof of concept, hierarchically porous TiO_2 was used as the anode in a lithium ion battery and compared with mesoporous TiO_2. The hierarchical TiO_2 exhibited high reversible capacity and excellent rate capability that could be attributed to the continuously interconnected macropores, which facilitate mass transport of electrolytes.

RESULTS AND DISCUSSION

Combined Hierarchical Assembly of Micro- and Macrophase Separation. The simplified free energy of mixing multiple components (ΔG_m) is given by

$$\Delta G_m = \Delta H_m - T\Delta S_m \quad (1)$$

where ΔH_m is the enthalpy of mixing and $T\Delta S_m$ is the entropy of mixing. This relationship indicates that the polymerization of any constituents decreases ΔS_m by reducing the number of degrees of freedom in the mixture, rendering ΔG_m less negative or even positive to induce phase separation ($\Delta G_m > 0$ causes demixing). In a similar manner, when reactive species are involved in BCP self-assembly, cross-linking and condensation concurrently occur; this process imparts a thermodynamic driving force for macrophase separation (i.e., chemically induced SD).[15b]

The key requirements to drive simultaneous integration of both micro- and macrophase separation are control of the condensation rates of the precursors and the interactions between the BCP and the precursors. First, a strongly segregating BCP is desirable to achieve a well-defined interface that enables hydrophilic species to be selectively incorporated

dx.doi.org/10.1021/ja5091172 | J. Am. Chem. Soc. 2014, 136, 16066–16072

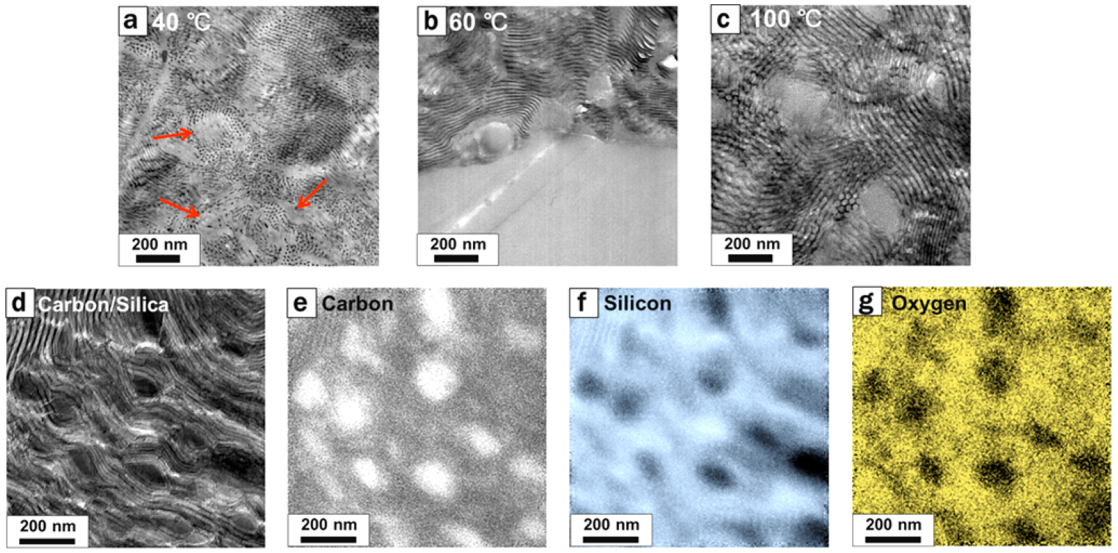

Figure 2. Structural evolution of phase separation in the resol/silicate/PEO-*b*-PS blend. (a–c) To visualize the process of hierarchical assembly, we used microtome sections for TEM measurements. Shown are TEM images of the blend (a) after solvent evaporation at 40 °C, (b) after thermal curing at 60 °C, and (c) after thermal curing at 100 °C. (d) Carbonization was conducted for EELS mapping to confirm the distribution of resol and silicates in the hybrid after thermal curing. (e–g) EELS mapping results for (e) carbon, (f) silicon, and (g) oxygen.

within the counterpart of the BCP. Second, the inorganic component should be able to interact with the hydrophilic block of the BCP without macrophase separation, i.e., mixing of the inorganic component with the BCP should be driven by favorable enthalpic interactions such as dipole–dipole, ion–ion, and hydrogen-bonding interactions. In addition, inorganic condensation should be retarded by complexation, acidification, or the use of nonaqueous solvents with controlled water contents to inhibit macrophase separation.[20] Third, unlike the inorganic species, the macrophase separation of the organic additive should be promoted without disrupting the self-organization of the BCP phase. For this purpose, polymerizable organic additives would be favorable to induce macrophase separation by in situ polymerization.[15b,21]

Here, we report CHAMPS, a simple yet versatile and powerful method to synthesize hierarchically porous inorganic materials that meets the requirements outlined in the preceding paragraph. As a first demonstration of CHAMPS, we employed a strongly segregating amphiphilic BCP, poly(ethylene oxide)-*block*-poly(styrene) (PEO-*b*-PS) (number-average molecular weight M_n = 36 kg mol^{-1}, 13.9 wt % PEO) as a structure-directing agent, phenol–formaldehyde resin (resol) as an additive that induces macrophase separation, and tetraethyl orthosilicate (TEOS) as a silica source in a highly acidic tetrahydrofuran (THF)/H_2O solution (Figure 1a). A small amount of concentrated HCl (35–37 wt % in H_2O) hydrolyses TEOS to form silicate oligomers and also initiates self-polymerization of resol. During solvent evaporation at 40 °C, the blends start to undergo macrophase separation into a resol-rich phase and a (resol/silicate/PEO-*b*-PS)-rich phase (Figure 1b). Meanwhile, silicates (hydrolyzed $M(OR)_xOH_y$) and part of the resol are incorporated into the PEO block by hydrogen bonding to form an ordered mesostructure by microphase separation (Figure 1d). Polymerizing resol segregates out to form a resol-rich core around which the mesostructure grows (Figure 1e). Subsequent thermopolymerization at 100 °C further ensures the structural integrity of both phases and freezes the overall frameworks, providing highly ordered hierarchical nanostructures. After resol and PEO-*b*-PS are removed by calcination at 600 °C, three-dimensionally interconnected ordered meso/macroporous silica is produced (Figure 1c). This strategy was successfully extended to the synthesis of hierarchically porous TiO_2.

Resol is synthesized by the reaction of phenol with excess formaldehyde under alkaline conditions. It consists of two to four phenols connected by methylene bridges, with a molecular weight of <500 g mol^{-1}, and can be cured by application of heat or addition of acid, which catalyze condensation of the methylol groups (Figure 1e).[22] Notably, resol has numerous hydroxyl and methylol groups that enable it to coassemble with amphiphilic BCPs by hydrogen bonding; therefore, resol has been widely adopted as a building block for the synthesis of ordered mesoporous carbon[23] and multicomponent composite materials.[18c,24]

The strongly acidic environment adjusted using HCl has two functions. One is to hinder inorganic condensation by protonation of the M–OH species, thereby leading to the formation of small hydrophilic inorganic oligomers that can favorably mix with the PEO block. The other is to act as an acid catalyst that accelerates the polymerization of resol, which decreases the interaction between resol and the BCP but increases self-aggregation of resol, resulting in the formation of resol-rich macrodomains. As a preliminary experiment, we employed a resol/HCl/THF solution in an EISA process at 40 °C. After solvent evaporation, a film made of resol was obtained and could be scraped off because of its enhanced mechanical strength (Supporting Figure S1). This observation indicates that resol polymerizes under strongly acidic conditions, although it is a stable, viscous liquid and is difficult to polymerize at temperatures below 60 °C.

The HCl-to-resol (H/R) ratio by weight was tuned in a series of experiments to determine the effect of resol polymerization on structure formation. When the H/R ratio was low or when dilute (0.1 M) HCl was used, ordered mesoporous silica was obtained (Supporting Figure S2), whereas an excess of HCl resulted in disordered and unstructured silica (Supporting Figure S3). The optimal H/R

dx.doi.org/10.1021/ja5091172 | J. Am. Chem. Soc. 2014, 136, 16066–16072

ratio for the formation of hierarchical silica with an ordered structure was determined to be 1−3.

At an H/R ratio of 2, we investigated the structural evolution of the phase separation in resol/silicate/PEO_{118}-*b*-PS_{298} blends using dynamic light scattering (DLS) and transmission electron microscopy (TEM). In the initial solution, all of the reactants were homogeneously dissolved without precipitation, and the solution contained only small particles with hydrodynamic diameters of <10 nm, corresponding to PEO-*b*-PS unimers (Supporting Figure S4). This DLS profile suggests that the degree of polymerization of resol was negligible and that no aggregates formed in the reaction solution. The solution was poured into a glass dish and held at 40 °C for several hours to evaporate volatile components (EISA) and then thermopolymerized (cured) at temperatures above 60 °C. After EISA at 40 °C, only ill-defined nanostructures were observed, but mesostructures composed of condensed silicate oligomers (darker part) developed, as did segregated macrodomains of polymeric components (Figure 2a). Subsequent curing at elevated temperatures increased the segregation strength as a result of polymerization of resol, allowing structural evolution into highly organized scaffolds.[25] Upon heating to 100 °C, silicate oligomers cross-linked to each other and more resol was driven out of the BCP phase (Figure 2b,c). To confirm the distribution of resol and silicates in the as-made hybrid material, we carbonized it at 700 °C (Figure 2d); electron energy loss spectroscopy (EELS) detected the elemental components of the carbon/silica composites and revealed the distributions of carbon (i.e., resol), silicon, and oxygen (Figure 2e−g). The carbon was homogeneously distributed in ordered mesoporous domains and was also densely concentrated in macrophase-separated domains that had sizes of hundreds of nanometers (Figure 2e). Silicon and oxygen were mostly dispersed within the ordered mesoporous frameworks, not in macrodomains. These results from DLS, TEM, and EELS indicate that hierarchical nanostructures steadily develop during EISA and curing, thereby resulting in macrophase separation of the blends into a resol-rich phase and a (resol/silicate/PEO-*b*-PS)-rich phase.

Hierarchically Porous Silica. Hierarchically porous silica (h-SiO_2) was obtained after calcination at 600 °C, as shown by scanning electron microscopy (SEM) (Figure 3a,b). Removal of resol-rich phases led to the formation of continuous macropores on the scale of hundreds of nanometers that were rather homogeneously distributed throughout the frameworks. In addition, the thermally decomposed PEO-*b*-PS left a well-defined mesostructure with cylindrical channels. Notably, the macropores were highly accessible from the mesopores, creating three-dimensionally interconnected ordered networks of macropores and mesopores (Figure 3a−c and Supporting Figure S5).

Small-angle X-ray scattering (SAXS) patterns were obtained for the as-made hybrid after thermal curing and for h-SiO_2 after calcination (Figure 3d). All of the peaks were shifted to larger q values because of framework shrinkage during the removal of the organic species by calcination. Both patterns have higher-order scattering peaks at angular positions of $\sqrt{3}$ and $\sqrt{4}$ relative to the first-order maximum; these can be assigned to the reflections of 2D hexagonal structures (*p6mm*). These well-resolved reflections indicate that h-SiO_2 has a long-range-ordered mesostructure after suffering framework shrinkage upon calcination.

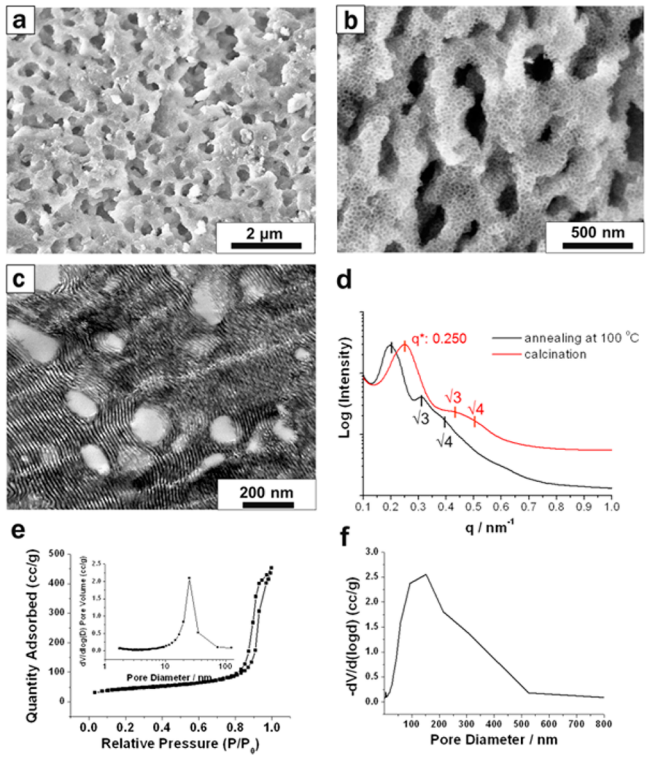

Figure 3. Characterization of hierarchically porous silica (h-SiO_2). (a, b) SEM images of h-SiO_2 on different length scales. (c) TEM image of microtomed h-SiO_2 with a section thickness of 100 nm. (d) SAXS patterns of the as-made hybrid after thermal annealing at 100 °C and h-SiO_2 after calcination. (e) N_2 physisorption isotherm and (inset) mesopore size distribution. From the adsorption branch of the isotherm, the mesopore size distribution was determined using the Barrett−Joyner−Halenda (BJH) method. (f) Macropore size distribution determined by mercury intrusion porosimetry.

The nitrogen physisorption isotherm of h-SiO_2 (Figure 3e) corresponds to a type-IV curve with a sharp adsorption near P/P_0 = 0.95, implying that uniform mesopores are dominant. The mesopores have a narrow size distribution with a mean diameter of 25 nm (Figure 3e inset). The specific surface area and mesopore volume were estimated to be 158 $m^2\ g^{-1}$ and 0.70 $cm^3\ g^{-1}$, respectively. Mercury intrusion porosimetry revealed that h-SiO_2 is composed of multiple levels of macropore sizes ranging from 50 to 400 nm with average diameter of 150 nm (Figure 3f). This result agrees with the SEM and TEM observations. The total intrusion volume of h-SiO_2 was 2.56 $cm^3\ g^{-1}$, which is comparable to or even larger than that of silica prepared by colloidal templating.[12,13b]

To unveil the nonperiodic 3D macrostructures of h-SiO_2, we used nanoscale X-ray computed tomography (nanoCT),[26] which provides X-ray absorption contrast between the materials and the porous regions. Focused ion beam milling was used to prepare specimens for nanoCT measurements (Supporting Figure S6).

Because of the limited resolution, nanoCT identified only macrodomains. The 3D-reconstructed image of h-SiO_2 showed a disordered structure (Figure 4a and Supporting Movie S1). To reveal the structural characteristics of this complex disordered macrostructure, it was further analyzed using a strut-thinning algorithm.[27] The zoomed images of h-SiO_2 (Figure 4b) and the resulting skeletal networks for the materials (blue struts in Figure 4c) and the macropores (red

dx.doi.org/10.1021/ja5091172 | J. Am. Chem. Soc. 2014, 136, 16066−16072

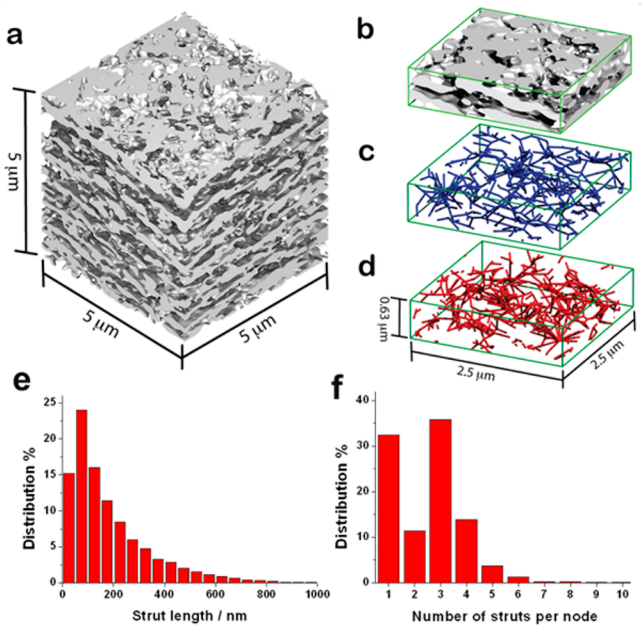

Figure 4. Macrostructure characterization of h-SiO_2. (a) Isosurface visualization of a 3D tomography reconstruction using nanoCT. (b–d) Structural characteristics of the macrostructure were analyzed with a strut-thinning algorithm, which transforms complex 3D network structures into simplified skeletal networks. Shown are zoomed images of (b) the macrostructure, (c) the skeletal networks for the materials region, and (d) the skeletal networks for the porous region. (e, f) Quantitative structural assessments of skeletal networks for the porous region: (e) distribution of node-to-node distances; (f) population distribution of struts per node.

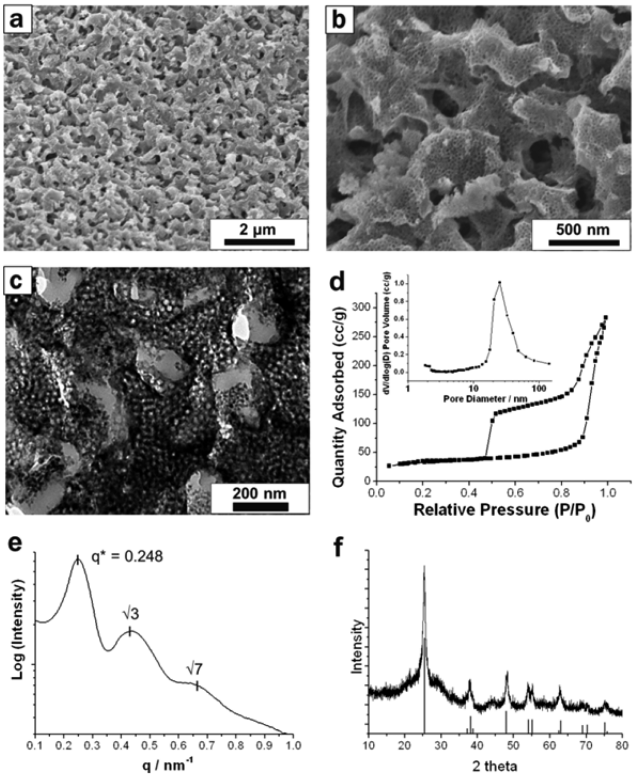

Figure 5. Characterization of hierarchically porous TiO_2-SiO_2-1 (denoted as h-TiSi-1). (a, b) SEM images of h-TiSi-1 on different length scales. (c) Microtomed TEM image of h-TiSi-1 with a section thickness of 100 nm. (d) N_2 physisorption isotherm and (inset) mesopore size distribution. (e) SAXS pattern of h-TiSi-1 after calcination. (f) XRD pattern corresponding to anatase TiO_2 (JCPDS no. 78-2486) and amorphous SiO_2.

struts in Figure 4d) exhibited a highly interconnected, cocontinuous nature. It should be mentioned that the continuous macropores are of great interest because they can increase the accessibility of small chemical species to mesoscopic surfaces in hierarchical materials compared with mesoporous materials. The network analyses further provided information on the size distribution and the degree of complexity of the porous networks. The largest population in the size distribution ranged between 50 and 100 nm (Figure 4e). Trivalent nodes were most common, and more crowded nodes were also observed, although monovalent nodes showed a high population (Figure 4f). It should be noted that some of the mono- and divalent nodes originate from artifacts on the edges of the zoomed volume. All of the results from nanoCT corroborate the unique formation mechanism of CHAMPS that is associated with in situ curing of resol (i.e., chemically induced SD).

Hierarchically Porous Metal Oxides with High Crystallinity. The EISA method for the preparation of mesoporous crystalline oxide materials has been extensively studied, and its ability to control pore structures, morphologies, and compositions has become well-established. Because it is based on EISA, CHAMPS can provide pathways for the preparation of crystalline metal oxides with hierarchical architectures. As a representative, we synthesized hierarchically porous TiO_2 by adding a titanium source to the initial h-SiO_2 synthetic solution and then calcined it at 600 °C. Two types of TiO_2 with different macroporosities were synthesized by changing the amount of resol. h-TiO_2-SiO_2-1 (h-TiSi-1) showed bicontinuously interconnected meso/macroporous networks (Figure 5a–c and Supporting Figure S7). Continuous macropores with sizes of 100–200 nm were well-developed throughout the entire scaffold composed of ordered mesopores. h-TiSi-1 had uniform mesopores with a size of 25 nm and a specific surface area of 114 m^2 g^{-1}. The SAXS pattern showed higher-order reflections at angular positions of $\sqrt{3}$ and $\sqrt{7}$, which are indicative of a hexagonal structure (Figure 5e). The X-ray diffraction (XRD) result (Figure 5f) corresponds to the anatase TiO_2 phase with broad amorphous SiO_2 peaks. TiO_2 was in a crystalline phase, and the average crystallite size was determined to be 10.2 nm using the Debye–Scherrer equation. Amorphous silica improved the mechanical and thermal stability, and thus, the original nanostructures of h-TiSi remained intact during crystallization at high temperature.[28]

To demonstrate the ability to control the macroporosity, the amount of resol was tuned; decreasing the resol content under the synthetic conditions for h-TiSi-1 led to the formation of h-TiSi-2 with smaller macropores (<100 nm; Figure 6a–c and Supporting Figure S8). Similar to h-TiSi-1, h-TiSi-2 also showed continuous macroporous scaffolds with ordered hexagonal mesostructures (Figure 6d,e) and an XRD pattern corresponding to a crystalline anatase TiO_2 phase (Figure 6f). The average crystallite size was estimated to be 11.2 nm, which is similar to the wall thickness (~12 nm) (Supporting Table S1). This indicates that the walls are in a crystalline state rather than consisting of nanocrystalline materials embedded in amorphous walls.[29]

To verify the structural merits of hierarchical porosity, h-TiO_2 was derived from h-TiSi-2 by NaOH etching and then

dx.doi.org/10.1021/ja5091172 | J. Am. Chem. Soc. 2014, 136, 16066–16072

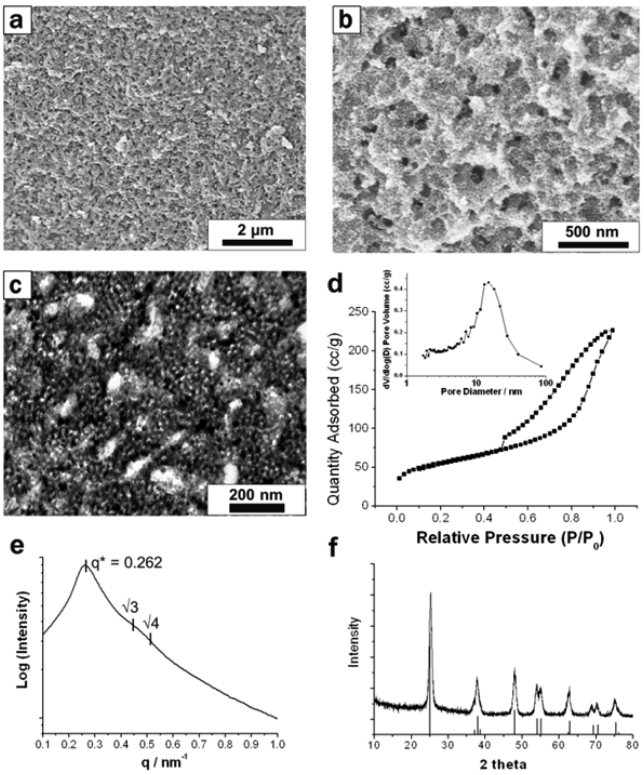

Figure 6. Characterization of hierarchically porous TiO_2-SiO_2-2 (denoted as h-TiSi-2). (a, b) SEM images of h-TiSi-2 on different length scales. (c) TEM image of microtomed h-TiSi-2 with a section thickness of 100 nm. (d) N_2 physisorption isotherm and (inset) mesopore size distribution. (e) SAXS pattern of h-TiSi-2 after calcination. (f) XRD pattern corresponding to anatase TiO_2 after removal of SiO_2.

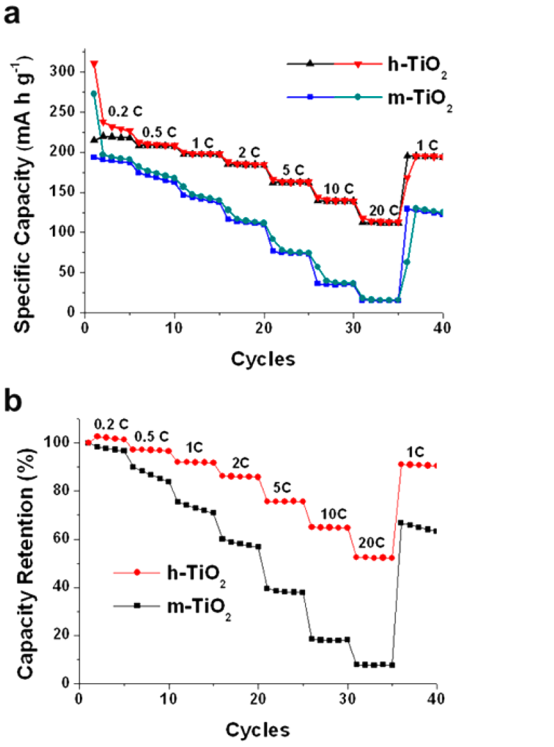

Figure 7. Electrochemical performance of silica-removed h-TiO_2 and m-TiO_2 as anodes in lithium ion batteries at current densities between 0.2 and 20 C rate (1 C = 167.5 mA g^{-1}). (a) Charge–discharge capacity values. (b) Capacity retention plots.

used as an anode in a lithium ion battery. It is well-known that the nanostructure of an electrode material affects its electrochemical properties.[30] The interconnected meso/macroporous nature of h-TiO_2 was well-retained with a minor structural deformation after silica removal (Supporting Figure S9). For comparison, mesoporous TiO_2 (m-TiO_2) was also prepared (Supporting Figure S10).[29b] The physicochemical properties of all of the hierarchical and mesoporous materials are summarized in Supporting Table S1.

h-TiO_2/Li and m-TiO_2/Li coin cells were assembled for galvanostatic charge–discharge tests over the potential range from 1.0 to 3.0 V vs Li/Li^+ (Supporting Figure S11). The h-TiO_2/Li cell exhibited a reversible capacity of 215 mA h g^{-1}, which is larger than that of m-TiO_2 (194 mA h g^{-1}) at 0.2 C rate (Figure 7a). Moreover, the h-TiO_2 electrode showed better rate capability as the C rate increased. The reversible capacity of the h-TiO_2 electrode was 113 mA h g^{-1} at 20 C rate (m-TiO_2: 15 mA h g^{-1}). The difference in rate performance is noticeable when the capacity values are normalized by their first discharge capacities (Figure 7b). For instance, h-TiO_2 retained 52.6% of its capacity, whereas m-TiO_2 retained only 8% at 20 C rate. Since the controlled factors, such as mesopore size, surface area, wall thickness, and average crystallite size, are almost identical in h-TiO_2 and m-TiO_2 (Supporting Table S1), the high reversible capacity and excellent rate performance of the h-TiO_2 electrode could be attributed to the continuously interconnected macropores. As electrolyte reservoirs, macropores provide easy wettability and facilitate mass transport of electrolytes, thereby resulting in fast response at high C rates.[30] The fast kinetics of the h-TiO_2 electrode was also supported by electrochemical impedance spectroscopy (EIS) analysis (Supporting Figure S12a). The data were collected with a symmetric cell (SC) configuration. In plots of imaginary capacitance, the h-TiO_2 SC showed higher peak frequency than did the m-TiO_2 SC (Supporting Figure S12b). This result indicates that macropores make ionic conduction easier in the h-TiO_2 electrode than in m-TiO_2 electrode.

■ CONCLUSIONS

We have developed CHAMPS, a simple and versatile one-pot method for the synthesis of inorganic oxide materials with multiscale porosity. Inorganic species and a portion of the resol were incorporated in the PEO block by hydrogen bonding, giving rise to mesostructures, while the polymerizing resol segregated out to form resol-rich macrodomains. Resol participates in both the micro- and macrophase separation, generating three-dimensionally interconnected macropores after calcination. The CHAMPS approach covers not only silica but also transition-metal oxides and provides direct access to hierarchically porous oxide materials, which have immense potential for applications that are limited by mass-transport capacity. This approach expands the base of conventional BCP self-assembly from mesostructures to hierarchically porous structures and fully utilizes the complex phase behavior of multicomponent blends for the design of unique nanostructures. Thus, it should attract broad interest from researchers in materials science and polymer science.

dx.doi.org/10.1021/ja5091172 | J. Am. Chem. Soc. 2014, 136, 16066–16072

■ ASSOCIATED CONTENT

Supporting Information

Experimental details, materials characterization, electrochemical characterization, and supporting data. This material is available free of charge via the Internet at http://pubs.acs.org.

■ AUTHOR INFORMATION

Corresponding Author

jinwoo03@postech.ac.kr

Notes

The authors declare no competing financial interest.

■ ACKNOWLEDGMENTS

This research was supported by the Basic Science Research Program through the National Research Foundation (NRF) funded by the Ministry of Science, ICT and Future Planning (2012R1A2A2A01002879 and 2013R1A1A2074550). SAXS measurements were carried out on the 4C SAXS beamline at Pohang Light Source II.

■ REFERENCES

(1) (a) Sanchez, C.; Arribart, H.; Guille, M. M. G. *Nat. Mater.* **2005**, *4*, 277−288. (b) Bae, W.-G.; Kim, H. N.; Kim, D.; Park, S.-H.; Jeong, H. E.; Suh, K.-Y. *Adv. Mater.* **2014**, *26*, 675−700.

(2) Yang, P.; Deng, T.; Zhao, D.; Feng, P.; Pine, D.; Chmelka, B. F.; Whitesides, G. M.; Stucky, G. D. *Science* **1998**, *282*, 2244−2246.

(3) Nakanishi, K.; Tanaka, N. *Acc. Chem. Res.* **2007**, *40*, 863−873.

(4) Parlett, C. M.; Wilson, K.; Lee, A. F. *Chem. Soc. Rev.* **2013**, *42*, 3876−3893.

(5) Li, Y.; Fu, Z. Y.; Su, B. L. *Adv. Funct. Mater.* **2012**, *22*, 4634−4667.

(6) Kresge, C.; Leonowicz, M.; Roth, W.; Vartuli, J.; Beck, J. *Nature* **1992**, *359*, 710−712.

(7) Attard, G. S.; Glyde, J. C.; Göltner, C. G. *Nature* **1995**, *378*, 366−368.

(8) Schüth, F. *Angew. Chem, Int. Ed.* **2003**, *42*, 3604−3622.

(9) Brinker, C. J.; Lu, Y.; Sellinger, A.; Fan, H. *Adv. Mater.* **1999**, *11*, 579−585.

(10) Li, X.; Jiang, J.; Wang, Y.; Nie, X.; Qu, F. *J. Sol-Gel Sci. Technol.* **2010**, *56*, 75−81.

(11) Xue, C.; Wang, J.; Tu, B.; Zhao, D. *Chem. Mater.* **2010**, *22*, 494−503.

(12) Stein, A.; Li, F.; Denny, N. R. *Chem. Mater.* **2008**, *20*, 649−666.

(13) (a) Petkovich, N. D.; Stein, A. *Chem. Soc. Rev.* **2013**, *42*, 3721−3739. (b) Kuang, D.; Brezesinski, T.; Smarsly, B. *J. Am. Chem. Soc.* **2004**, *126*, 10534−10535. (c) Mandlmeier, B.; Szeifert, J. M.; Fattakhova-Rohlfing, D.; Amenitsch, H.; Bein, T. *J. Am. Chem. Soc.* **2011**, *133*, 17274−17282. (d) Dacquin, J.-P.; Dhainaut, J.; Duprez, D.; Royer, S.; Lee, A. F.; Wilson, K. *J. Am. Chem. Soc.* **2009**, *131*, 12896−12897. (e) Shi, Y.; Zhang, F.; Hu, Y.-S.; Sun, X.; Zhang, Y.; Lee, H. I.; Chen, L.; Stucky, G. D. *J. Am. Chem. Soc.* **2010**, *132*, 5552−5553. (f) Falcaro, P.; Malfatti, L.; Kidchob, T.; Giannini, G.; Falqui, A.; Casula, M. F.; Amenitsch, H.; Marmiroli, B.; Grenci, G.; Innocenzi, P. *Chem. Mater.* **2009**, *21*, 2055−2061. (g) Sun, J.; Shan, Z.; Maschmeyer, T.; Moulijn, J. A.; Coppens, M.-O. *Chem. Commun.* **2001**, 2670−2671. (h) Song, M.-G.; Kim, J.-Y.; Cho, S.-H.; Kim, J.-D. *Langmuir* **2002**, *18*, 6110−6115.

(14) (a) Cahn, J. W. *Acta Metall.* **1961**, *9*, 795−801. (b) Cahn, J. W. *J. Chem. Phys.* **1965**, *42*, 93−99. (c) Langer, J. *Ann. Phys.* **1971**, *65*, 53−86.

(15) (a) Bates, F. S. *Science* **1991**, *251*, 898−905. (b) Inoue, T. *Prog. Polym. Sci.* **1995**, *20*, 119−153.

(16) Sai, H.; Tan, K. W.; Hur, K.; Asenath-Smith, E.; Hovden, R.; Jiang, Y.; Riccio, M.; Muller, D. A.; Elser, V.; Estroff, L. A.; Gruner, S. M.; Wiesner, U. *Science* **2013**, *341*, 530−534.

(17) (a) Warren, S. C.; DiSalvo, F. J.; Wiesner, U. *Nat. Mater.* **2007**, *6*, 156−161. (b) Kang, E.; Jung, H.; Park, J. G.; Kwon, S.; Shim, J.; Sai, H.; Wiesner, U.; Kim, J. K.; Lee, J. *ACS Nano* **2011**, *5*, 1018−1025.

(18) (a) Jeon, K.-J.; Roe, R.-J. *Macromolecules* **1994**, *27*, 2439−2447. (b) Koizumi, S.; Hasegawa, H.; Hashimoto, T. *Macromolecules* **1994**, *27*, 6532−6540. (c) Hwang, J.; Woo, S. H.; Shim, J.; Jo, C.; Lee, K. T.; Lee, J. *ACS Nano* **2013**, *7*, 1036−1044.

(19) Deng, Y.; Liu, J.; Liu, C.; Gu, D.; Sun, Z.; Wei, J.; Zhang, J.; Zhang, L.; Tu, B.; Zhao, D. *Chem. Mater.* **2008**, *20*, 7281−7286.

(20) Soler-Illia, G. J. d. A.; Sanchez, C.; Lebeau, B.; Patarin, J. *Chem. Rev.* **2002**, *102*, 4093−4138.

(21) Lipic, P. M.; Bates, F. S.; Hillmyer, M. A. *J. Am. Chem. Soc.* **1998**, *120*, 8963−8970.

(22) Gardziella, A.; Pilato, L. A.; Knop, A. *Phenolic Resins: Chemistry, Applications, Standardization, Safety and Ecology*; Springer: Berlin, 2000.

(23) Meng, Y.; Gu, D.; Zhang, F.; Shi, Y.; Cheng, L.; Feng, D.; Wu, Z.; Chen, Z.; Wan, Y.; Stein, A.; Zhao, D. *Chem. Mater.* **2006**, *18*, 4447−4464.

(24) (a) Shim, J.; Lee, J.; Ye, Y.; Hwang, J.; Kim, S. K.; Lim, T. H.; Wiesner, U. *ACS Nano* **2012**, *6*, 6870−6881. (b) Jo, C.; Hwang, J.; Song, H.; Dao, A. H.; Kim, Y. T.; Lee, S. H.; Hong, S. W.; Yoon, S.; Lee, J. *Adv. Funct. Mater.* **2013**, *23*, 3747−3754.

(25) Schuster, J.; Köhn, R.; Döblinger, M.; Keilbach, A.; Amenitsch, H.; Bein, T. *J. Am. Chem. Soc.* **2012**, *134*, 11136−11145.

(26) Lim, J.; Kim, H.; Park, S. *J. Synchrotron Radiat.* **2014**, *21*, 827−831.

(27) Lee, T.-C.; Kashyap, R. L.; Chu, C.-N. *CVGIP Graphical Models Image Process.* **1994**, *56*, 462−478.

(28) Dong, W.; Sun, Y.; Lee, C. W.; Hua, W.; Lu, X.; Shi, Y.; Zhang, S.; Chen, J.; Zhao, D. *J. Am. Chem. Soc.* **2007**, *129*, 13894−13904.

(29) (a) Hwang, J.; Kim, J.; Ramasamy, E.; Choi, W.; Lee, J. *Microporous Mesoporous Mater.* **2011**, *143*, 149−156. (b) Lee, J.; Orilall, M.; Warren, S.; Kamperman, M.; DiSalvo, F.; Wiesner, U. *Nat. Mater.* **2008**, *7*, 222−228.

(30) (a) Mun, Y.; Jo, C.; Hyeon, T.; Lee, J.; Ha, K.-S.; Jun, K.-W.; Lee, S.-H.; Hong, S.-W.; Lee, H. I.; Yoon, S. *Carbon* **2013**, *64*, 391−402. (b) Wang, D. W.; Li, F.; Liu, M.; Lu, G. Q.; Cheng, H. M. *Angew. Chem., Int. Ed.* **2008**, *47*, 373−376. (c) Wu, Z.-S.; Sun, Y.; Tan, Y.-Z.; Yang, S.; Feng, X.; Müllen, K. *J. Am. Chem. Soc.* **2012**, *134*, 19532−19535.